Ultra-Wideband Multi-Octave Planar Interconnect for Multi-Band THz Communications

Shuya Iwamatsu[1] · Muhsin Ali[2] · José Luis Fernández-Estévez[1] · Jonas Tebart[1] · Ashish Kumar[3] · Sumer Makhlouf[1] · Guillermo Carpintero[2,3] · Andreas Stöhr[1]

Abstract

An ultra-wideband (UWB) interconnect technology using indium phosphide (InP)-based transitions for coupling the output signals from terahertz (THz) photodiodes featuring coplanar waveguide (CPW) outputs to low-loss dielectric rod waveguides (DRWs) is presented. The motivation is to exploit the full bandwidth offered by THz photodiodes without limitations due to standard rectangular waveguide interfaces, e.g., for future high data rate THz communications. Full electromagnetic wave simulations are carried out to optimize the electrical performance of the proposed InP transitions in terms of operational bandwidth and coupling efficiency. The transitions are fabricated on 100-μm-thin InP and integrated with silicon (Si) DRWs. Experimental frequency domain characterizations demonstrate efficient THz signal coupling with a maximum coupling efficiency better than -2 dB. The measured 3-dB and 6-dB operational bandwidths of 185 GHz and 280 GHz, respectively, prove the multi-octave ultra-wideband features of the developed interconnect technology. The 6-dB operational bandwidth covers all waveguide bands between WR-12 to WR-3, i.e., a frequency range between 60 and 340 GHz. In addition, the multi-octave performances of the fabricated interconnects were successfully exploited in proof-of-concept THz communication experiments. Using intermediate frequency orthogonal frequency division multiplexing (OFDM), THz communications are demonstrated for several frequency bands using the same interconnect. Considering soft-decision forward error correction, error-free transmission with data rates of 24 Gbps at 80 GHz and 8 Gbps at 310 GHz is achieved.

✉ Andreas Stöhr
andreas.stoehr@uni-due.de

1   Center of Semiconductor Technology and Optoelectronics (ZHO), Optoelectronics Department, University of Duisburg-Essen, Lotharstr. 55, 47057 Duisburg, Germany

2   LeapWave Technologies, Leganés, 28919 Madrid, Spain

3   Department of Electronics Technology, University Carlos III of Madrid, Leganés, 28911 Madrid, Spain

1 Introduction

The demand for higher data rates is growing rapidly with the emergence of artificial intelligence (AI)-powered cloud computing, ever-increasing device connectivity, and richer content such as virtual reality (VR) and 8 K video [1]. To support these services, it is essential to overcome bandwidth limitations introduced by interconnect technologies such as wire bonding to enable ultra-high-speed communications of 100 Gbps or more, potentially 1 Tbps. In recent years, the terahertz (THz) frequency band has attracted increasing attention as a promising technology for communications [2, 3]. The advantage of THz waves is their substantial bandwidth. Therefore, ultra-wideband (UWB) communications and multi-band communications using frequency division multiplexing (FDM) schemes in the THz band are critical factors in achieving Tbps communication links [4]. Besides communications, the availability of the vast bandwidth plays a vital role in the development of high-resolution sensors for ranging [5], non-destructive imaging [6], 3D imaging [7], and THz spectroscopy for material identification from fingerprints [8–10].

Indium phosphide (InP)-based uni-traveling carrier photodiodes (UTC-PDs) have an enormous potential for such UWB applications owing to the multi-octave tunable THz signal generation enabled by the photomixing technique [11, 12]. The operating frequency can be easily selected by tuning the difference frequency of two tunable laser signals. Recently, InP-based UTC-PDs have exhibited UWB operation beyond 4 THz [13] and promising levels of output power, reaching over + 15 dBm at 77 GHz [14], + 3.4 dBm at 150 GHz [15], and − 0.6 dBm at 240 GHz [16]. However, the conventional packaging technology based on metallic rectangular waveguide (WR) interfaces or antennas limits the operational bandwidth of broadband THz-PDs [7, 8, 14–16]. On the other hand, although the use of silicon (Si) lenses enables UWB operation for free-space optics, their large physical size prevents planar integration into compact THz integrated circuits [17–19].

Figure 1 presents a conceptual schematic of an FDM-based onboard THz data link using an UWB transition interconnecting UWB THz UTC-PD transmitter (Tx) and THz UWB receiver (Rx). Contrary to WRs and Si lenses, planar dielectric waveguides [19–23] made of high-resistive (> 10 kΩ·cm) silicon (HR-Si) are very promising to cover the UWB operational frequency range in THz integrated circuits. The potential of dielectric rod waveguides (DRWs) as UWB antennas at 75–1100 GHz has been demonstrated [20]. Furthermore, the transmission loss of DRWs was found to be smaller than 0.087 dB/cm at 90–220 GHz in [21] and 0.059 dB at 260–390 GHz in [22] since there are no ohmic losses. All-intrinsic-silicon THz microphotonics systems using DRWs has been proposed for compact and broadband THz communication and spectroscopic sensor applications [22–27]. Thus, it is advantageous to integrate HR-Si DRWs with InP-based UTC-PDs through an efficient UWB transition. This will allow overcoming the WRs and Si lenses limitations and developing ultra-high-speed on-chip communication with the THz UWB UTC-PD Tx and UWB Rx, as
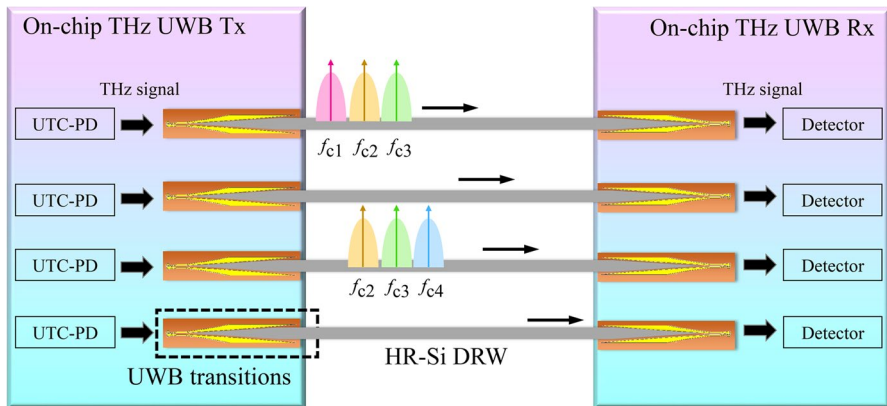
Fig. 1 Conceptual schematic of onboard THz data links based on frequency division multiplexing (FDM) schemes. Proposed interconnects, consisting of ultra-wideband (UWB) transitions and high-resistive silicon (HR-Si)-based dielectric rod waveguide (DRW) interconnect between on-chip THz-PD transmitter (Tx) and THz UWB receiver (Rx)

presented in Fig. 1. Usually, UTC-PDs feature 50-Ω planar transmission lines at the output, particularly coplanar waveguides (CPWs). This enables to couple the RF output power to other components, such as amplifiers or antennas.

We present, in this work, an UWB transition between InP-based CPWs and Si DRWs. The signal is coupled from the CPW to the DRW in two steps. First, a transition from CPW to coplanar stripline (CPS) is considered to ensure impedance matching and efficient coupling by considering enough contact surface for the DRW on the InP substrate. Then, the signal is further coupled to the DRW.

This paper is organized as follows: InP-based transition design and structure are described in Section 2. The device fabrication and assembly are explained in Section 3. Finally, a study on the coupling efficiency of the transition through the experiment is presented in Section 4. Communication experiments through the proposed interconnection are demonstrated at 80-GHz and 300-GHz bands in Section 5. Finally, this work concludes in Section 6.

2 InP-Based Tapered-Slot Transition

A wideband coupling technique to integrate InP-based UTC-PD with Si DRW is studied in this work. Figure 2 illustrates the concept of wideband coupling. As presented in Fig. 2(a), we couple the THz signal from the InP-based planar waveguide to the Si DRW by attaching the DRW to the middle of the tapered-slot transition with an exponential-curve profile [27]. Preliminary findings that tapered-slot transitions enable an efficient transition at WR-12 and WR-10 bands have been reported in [28]. The waveguide modes in the transition are gradually coupled to the Si DRW taper in the vertical direction, and the transferred modes are propagated into the Si DRW. In addition, a transition from CPW to CPS is included in the entire transition, as
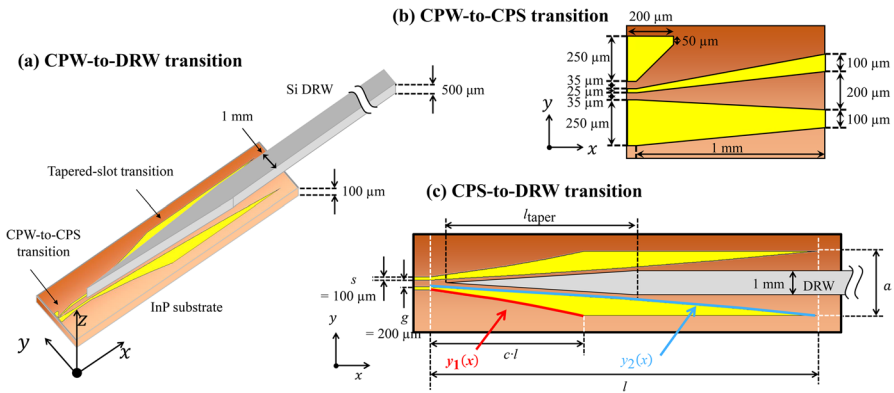
Fig. 2 Schematic of InP-based transition from coplanar waveguide (CPW) to Si dielectric rod waveguide (DRW). (**a**) 3D schematic of whole transition, consisting of CPW-to-coplanar stripline (CPS) transition, 1-mm-long straight CPS, and CPS-to-DRW transition. DRW taper is attached on the middle of the tapered-slot transition. (**b**) Top view of CPW-to-CPS transition. (**c**) Top view of CPS-to-DRW transition. Parameters of the tapered-slot transition design are shown

shown in Fig. 2(b). The CPW pads allow contact with ground-signal-ground (GSG) probes to characterize the transition and conduct communication experiments, which will be presented later. Moreover, since the UTC-PDs we have recently reported in [15, 16] have the same CPW pads as an output, the transition proposed here could be monolithically integrated with the UTC-PD in the future. The transition can be designed based on Eqs. (1) and (2)

$$y_1(x) = \left(\frac{a - g - 2s + 2}{2} \right)^{x/cl} + \frac{g}{2} + s - l, \qquad (1)$$

$$y_2(x) = \left(\frac{a - g + 2}{2} \right)^{x/l} + s - l, \qquad (2)$$

where a, c, and l are the aperture, curvature, and length of the transition, respectively, and s and g are the width of the signal line and ground of the CPS input. Equations (1) and (2) determine the inner and outer curves of the transition, which are shown in Fig. 2(c).

Regarding the DRW design, the cross section and each length of the linear taper l_{taper} and the straight section were fixed as 1.0×0.5 mm^2, 8 mm, and 45 mm, respectively, because it operates in the UWB range from approximately 65 GHz to beyond 300 GHz. The lower cutoff frequency was determined by the cross section of the DRW [29].

Table 1 shows the resulting parameters for the proposed transition after electromagnetic-wave simulations (using CST Studio Suite 2022). To optimize the parameters, firstly, the coupling efficiency of the CPS-to-DRW transition $\eta_{CPS \rightarrow DRW}$ is defined as

Table 1 Transition design parameters

CPS width	s	100 μm
CPS gap	g	200 μm
Transition aperture	a	2 mm
Transition length	l	12 mm
Transition curvature	c	0.4

$$\eta_{CPS \to DRW} = \frac{P_{WR} - IL_{DRW \to WR}}{P_{CPS}}, \qquad (3)$$

where P_{CPS} represents the power fed to the CPS input of the CPS-to-DRW transition, P_{WR} represents the power coupled to WR waveguides, and $IL_{DRW \to WR}$ is the insertion loss of the coupling part from the middle of the DRW to the WR waveguide, as illustrated in Fig. 3(a). This definition is applied to both the simulation and the measurement. For determining $IL_{DRW \to WR}$, we first simulated the total insertion loss of the DRW coupled to the WR waveguides on both sides and then divided this loss by two. The interconnect using the transition on the InP substrate and the Si DRW was thoroughly investigated in the simulations. As the aperture determines the lower cutoff frequency and the cross section of the DRW, a was selected as small as 2 mm to cover the 3-dB operational frequency range from 65 GHz, as shown in Fig. 3(b). For optimizing l, a trade-off between the coupling efficiency and the operational bandwidth was considered. The longer the transition, the more efficient the coupling is at lower frequencies, though the higher the metal loss is caused at higher frequencies. As shown in Fig. 3(c), l was determined as 12 mm as a result of taking the trade-off into account. The curvature c affects the coupling efficiency, which is barely the best at 0.4 up to around 200 GHz, as shown in Fig. 3(d). After the thorough optimization, we simulated a coupling efficiency of the CPW-to-DRW transition $\eta_{CPW \to DRW}$ from 60 to 350 GHz, which is defined as

$$\eta_{CPW \to DRW} = \frac{P_{WR} - IL_{DRW \to WR}}{P_{CPW}}, \qquad (4)$$

where P_{CPW} is the power fed to the CPW input of the CPW-to-DRW transition, as well as $\eta_{CPS \to DRW}$. Figure 4(a) presents the simulated results of the coupling efficiency. In the CPS-to-DRW transition, an efficient coupling with less than 1 dB loss can be seen in the frequency range from 70 to 190 GHz. In the same frequency range, the CPW-to-DRW transition has a coupling efficiency of approximately -2 dB. The difference between the two coupling efficiencies corresponds to the loss in the CPW-to-CPS transition. Figure 4(b) and (c) show the different losses contributing to the total coupling loss of the CPW-to-DRW transition and the E-field distributions at 80, 240, and 300 GHz. As can be seen, the coupling loss is mainly dominated by radiation loss, followed by metal loss. Compared to those losses, the reflection loss and the dielectric loss are less dominant, with < 0.5 dB and < 0.003 dB, respectively. Above 220 GHz, the coupling efficiency decreases with frequency and sharply drops at 220–250 GHz, primarily because of radiation loss. A peak of the radiation loss at 240 GHz corresponds to a drop in coupling efficiency (Fig. 4(b)). The cause of the
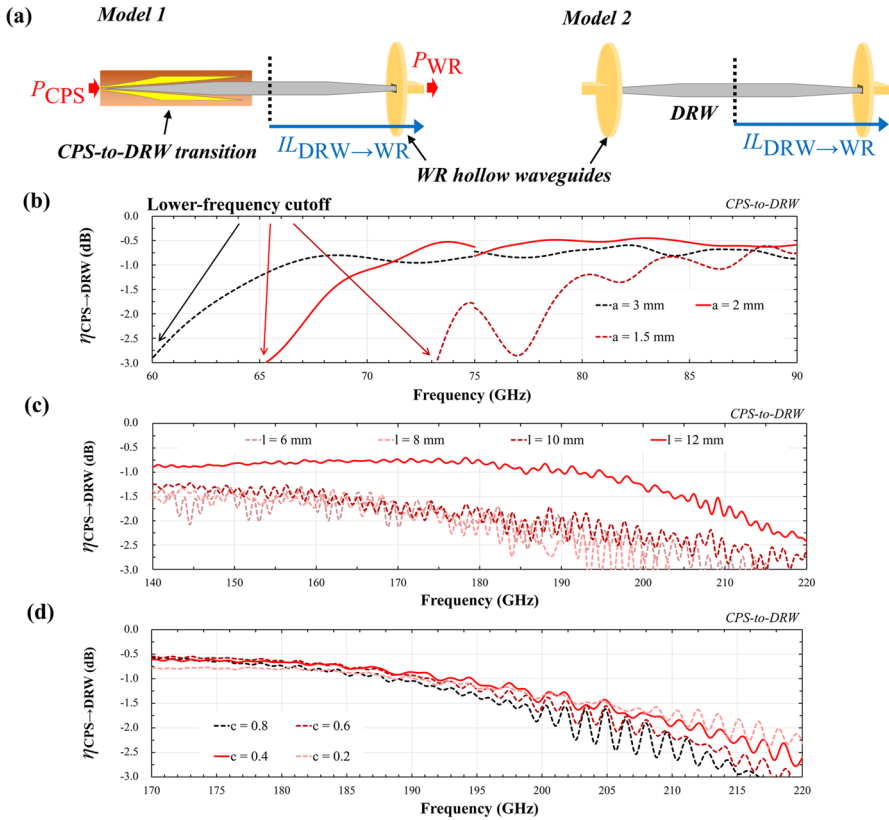
Fig. 3 Optimization of CPS-to-DRW tapered-slot transition design. (**a**) Schematic of two simulation models (CPS-to-WR transition and WR-to-DRW-to-WR transition). Simulated coupling efficiency of the CPS-to-DRW transition with different parameters swept, (**b**) the aperture, (**c**) the length, and (**d**) the curvature of the tapered-slot transition. Red solid lines in each graph show the coupling efficiency with the optimized parameters

sharp increase in radiation loss is a combination of two undesired mode excitations. The excitation of a substrate mode in the InP substrate is the one. We employ a 100-μm-thick InP substrate in this work so that we can handle the chip and assemble the device by hand. However, the right substrate thickness for higher-frequency operations is much smaller. The thickness of the InP substrate for the WR-3 band is 50 μm [30, 31]. Figure 5 shows the simulation results of three different CPW-to-DRW transitions with different InP substrate thicknesses and different thicknesses of Si DRWs. As shown in Fig. 5, no drop in the coupling efficiency or increase of the radiation loss can be seen at 220–250 GHz with a 50-μm-thick InP substrate, which is shifted to a higher frequency over 320 GHz. This indicates that introducing a 50-μm-thick InP substrate can suppress the substrate modes that cause significant radiation loss at the WR-3 band.
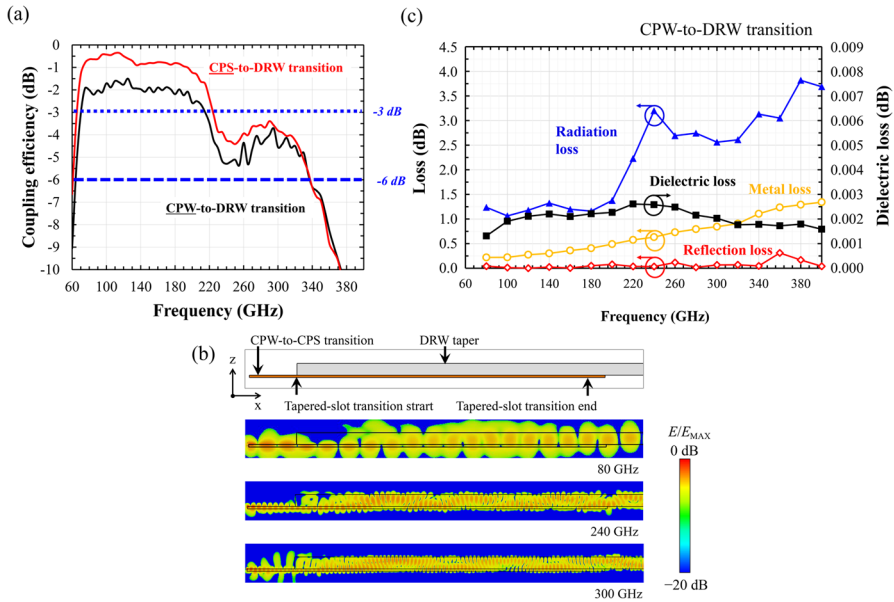
Fig. 4 (**a**) Simulation results of the CPS/CPW-to-DRW transition: (**a**) coupling efficiency, (**b**) different losses contributed to the coupling loss, and (**c**) E-field distributions at 80, 240, 300 GHz
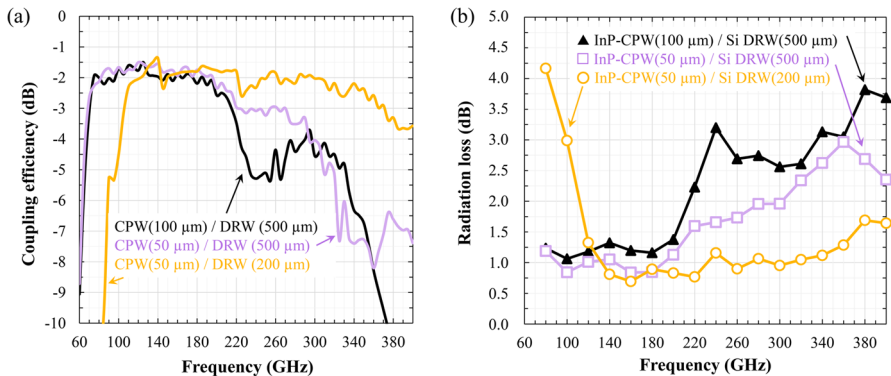

Fig. 5 Simulated (**a**) coupling efficiency and (**b**) radiation loss of different transitions with 100/50-μm-thick InP CPW and 500/200-μm-thick Si DRW

The other unnecessary modes excited in the transition are high-order modes. As Fig. 4(c) shows, modes are winding at 240 and 300 GHz. For the realization of UWB operation in both millimeter wave and THz frequency band, such as between WR-12 (60–90 GHz) and WR-3 bands, a 500-μm-thick Si DRW is employed; however, high-order modes start propagating in such a thick dielectric waveguide as the frequency increases and cause a significant interaction with the fundamental mode, leading an additional radiation loss. The frequency at which the high-order modes interfere with

the fundamental mode depends on the thickness of the Si DRW because the thicker Si DRW aggravates a symmetricity of the mode propagation in a vertical direction and increases the interference between different modes. To fix the asymmetrical mode propagations, a thinner Si DRW is desired, which is not introduced for keeping the UWB operational band from WR-12 band in this work. By improving the symmetricity, the frequency at which the high-order modes interact with the fundamental mode can be shifted. As can be seen from Fig. 5, the CPW-to-DRW transition on the 50-μm-thin InP substrate, using a 200-μm-thin DRW, removes the sharp increase of the radiation loss and improves the coupling efficiency at 220–250 GHz, although the lower cutoff is also shifted from approximately 65 to 90 GHz, limiting the operational band.

3 Chip Assembly and Fabrication

The designed tapered-slot transitions with 50-Ω CPW were fabricated on a 100-μm-thin InP substrate. Although a substrate-transfer fabrication process to keep the mechanical stability of 50-μm-thick InP chips was reported recently for developing a THz leaky-wave antenna for WR-3 band [31], the reported process could not be applied to this work because of a gold bonding layer and a thick Si transfer substrate. They were introduced for realizing the mechanical stability; however, the gold bonding layer on the bottom of the InP substrate would lead to a grounded CPW, causing a substantially worse coupling efficiency to the DRW. Even without the gold layer, a high-permittivity supporting substrate would increase the effective thickness of the transition and thus also cause a high coupling loss. The electrical field must be well confined to enable an efficient coupling from the transition to DRW. We, therefore, investigated two alternatives for supporting InP substrates with less influence on the coupling efficiency: One is an extremely low permittivity foam, ROHACELL 71 HF [32]. The other is the cyclic olefin copolymer (COC) plate, TOPAS 5013L-10 [33]. The permittivity of the ROHACELL and the COC is 1.09 and 2.35, respectively. The lower the substrate's permittivity, the less the coupling efficiency is affected.

We bonded the fabricated transition chip on the foam first. Then, the bonding was done manually by placing the chip on the top of the foam, covered with a benzocyclobutene (BCB) polymer by a spin coating process. Figure 6 shows the photograph of the fabricated chip before and after bonding on the foam. Because of the large surface roughness of the foam ($\sim \pm 200$ μm), the bonding was insufficient to keep the mechanical stability during the characterization with probe contacts. Hence, we employed the COC plate, which had a flat surface with a roughness of < 1 μm. The foam was used as supporting material for characterizing the coupler at 60–110 GHz, and the COC plate was used at 110–170 GHz and 250–350 GHz.

4 Measurement

We experimentally conducted THz signal coupling from InP CPW to Si DRW. Figure 7(a)–(e) show the experimental setups for characterizations at different frequency bands. The coupling efficiency was measured using WR-based equipment
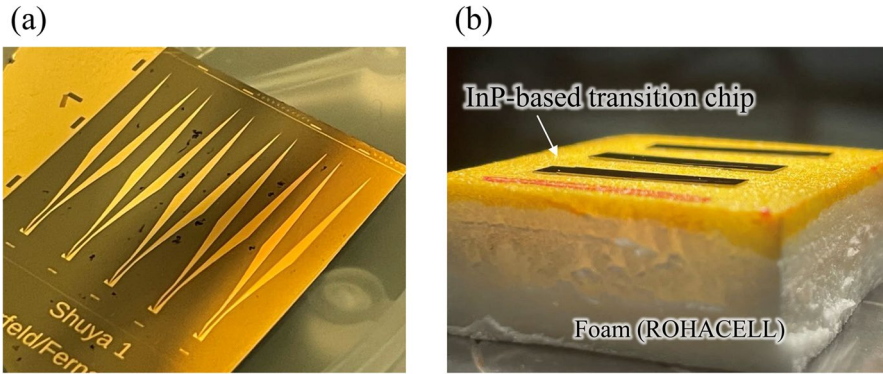
(a)   (b)

Fig. 6 Photograph of (**a**) the fabricated transitions on 100-μm-thin InP substrate and (**b**) the transition chips bonded on low permittivity foam, ROHACELL with a thickness of 4 mm

from 60 to 350 GHz, except for 170–250 GHz, where no THz source and GSG probe were available in our laboratories.

4.1 Vector Network Analyzer at 60–90 GHz

A vector network analyzer (VNA) (*Anritsu*, MS4647B) was used to characterize the coupling from 60 up to 90 GHz to determine the lower limit of the operational bandwidth. The signal from port 1 was fed to the transition through the GSG probe with less than 1.2 dB of insertion loss. At the receiving side, we employed a DRW probe with a DRW taper as its input/output interface [34] connected to port 2, as shown in Fig. 7(b). The calibration of the DRW probe was conducted by calculating the loss of the DRW probe from the measured S_{21} in a back-to-back
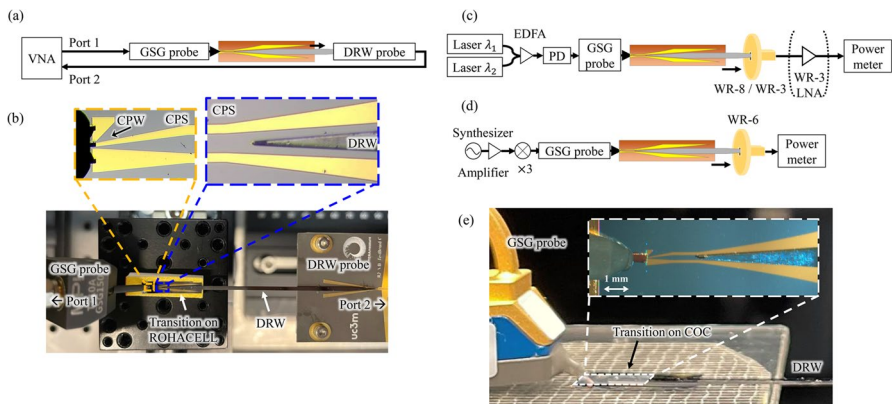

Fig. 7 Experimental setups for characterizing the transition at (**a**) 60–90, (**c**) 90–110 and 250–350 GHz, and (**d**) 110–170 GHz. Photographs of the experimental setups for the measurement at (**b**) 60–90 and (**e**) 110–170 GHz. WR-3 LNA was used only in the characterization at 250–350 GHz

configuration with two DRW probes first, and the calculated loss of one DRW probe was subtracted from the measured S_{21} in the total coupling efficiency of the transition measured in the end. As can be seen from Fig. 8, the lower frequency cutoff is around 65 GHz. For frequencies between 80 and 90 GHz, the coupling efficiency is about -2 dB. Both results agree well with the simulations.

4.2 Photodiodes and Power Meter at 90–110 GHz and 250–350 GHz

A PD with 1-mm coaxial output (*Finisar*, XPDV4121R-WF-FA), a J-band UTC-PD (*NTT Electronics*), an Erbium-doped fiber amplifier (EDFA), GSG probes, and a power meter (*VDI*, Erickson PM5) were used for characterizing the transition at 90–110 GHz and 250–350 GHz. Because the available output power from the UTC-PD was insufficient to measure the power through the transition and the DRW, a low-noise amplifier (LNA) (*Radiometer Physics*, H-LNA) with a maximum gain of 28 dB and a noise figure of 11 dB, operating at 250–350 GHz, was used additionally. For calibration, the loss in half of the straight section of DRW and the DRW linear taper inserted into the hollow waveguide were measured at each frequency band, and then, the coupling efficiency was obtained. The calculated coupling efficiency from the measurements is presented in Fig. 8. Even though a fluctuation of around 1–2 dB can be seen because of standing waves in the measurement configurations, The measured coupling efficiencies for the two transitions on ROHACELL and COC both agree well with simulations.
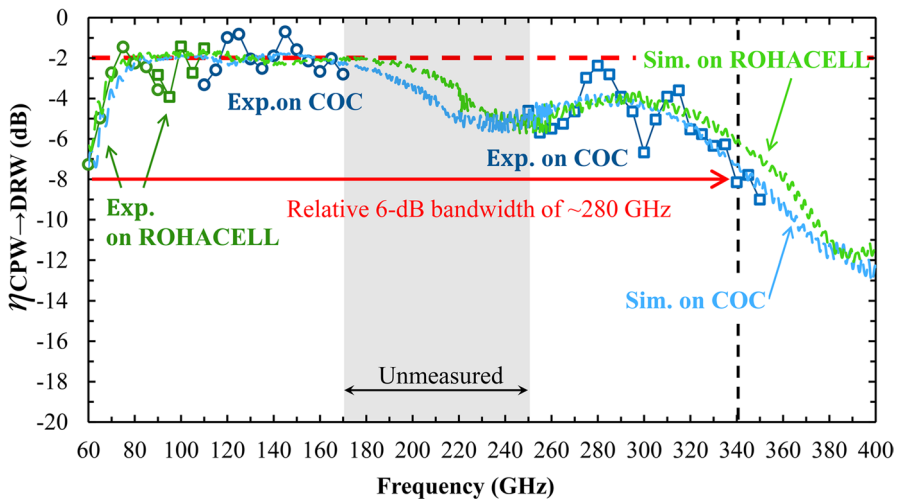

Fig. 8 Coupling efficiency of the CPW-to-DRW transition demonstrated at 60–110 GHz on ROHACELL (*green*) and 110–170 GHz and 250–350 GHz on COC plate (*blue*). The transition was not able to demonstrate the coupling at 170–250 GHz due to no equipment available

4.3　Frequency Multiplier and Power Meter at 110–170 GHz

A frequency multiplier (*VDI*) was used for tripling the signal frequency generated by a synthesizer (*Anritsu*, 68087B) to demonstrate the coupling at 110–170 GHz. As shown in Fig. 7(c), the frequency was swept from 33.83 to 56.33 GHz, and the amplified signal through a driver amplifier (*CENTELLAX*, OA5MVM) pumped the tripler. A WR-6 GSG probe connected to the tripler fed the THz signal to the transition chip, and the signal was coupled to the DRW through the transition. The WR-6 hollow waveguide is attached to the DRW and detects the coupled power with the power meter. As a result, the experiment at 110–170 GHz also demonstrated a coupling efficiency of approximately -2 dB, which agrees with the simulation.

The measured entire coupling efficiency of the CPW-to-DRW transition reveals a 3-dB and 6-dB operational bandwidth of approximately 185 and 280 GHz, starting from 65 to 250 GHz and 60 to 340 GHz, respectively. This corresponds to record high relative bandwidths of 114% and 140%, respectively. In addition, as Fig. 8 shows, there is a difference in the first roll-off in the simulated coupling efficiency between the ROHACELL and the COC plate, which the effective thickness change in the CPW-to-DRW transition could explain. Since the COC has a higher permittivity than the ROHACELL, the effective thickness of the transition chip is increased. Hence, the overall frequency response is shifted to lower frequencies. This is also true for the frequencies around 240 and 340 GHz, at which higher-order modes propagate.

5　Data Communications Experiments

As mentioned in Section 1, multi-band communications based on FDM are promising technologies for THz communication applications. After demonstrating the wide operating bandwidth of the interconnection using the DRW, we show a single-channel data transmission in the multi-frequency band using the DRW interconnect to exhibit the potential of FDM-based multi-channel communications.

5.1　DRW Interconnects at 80-GHz Band

A photonics-assisted wired communication using the transition and the DRW was demonstrated at 80 GHz. Figure 9 illustrates the block diagram of the communication experiment setup. The intermediate frequency orthogonal frequency division multiplexing (IF-OFDM) [35] based I-Q data signal is generated using a digital signal processing (DSP) routine. The number of sub-carriers in OFDM is 1024; each is modulated using a 4-QAM and 16-QAM signal format. The OFDM I-Q signal is generated using an arbitrary waveform generator (AWG) (*Keysight*, M9505A) at an intermediate frequency (IF) f_{IF} of 5 GHz. The IF signal is amplified by a medium power amplifier (MPA) (SHF810) and fed into a Mach-Zehnder modulator (MZM) (*Fujitsu*, FTM7938EZ) to modulate λ_1. The
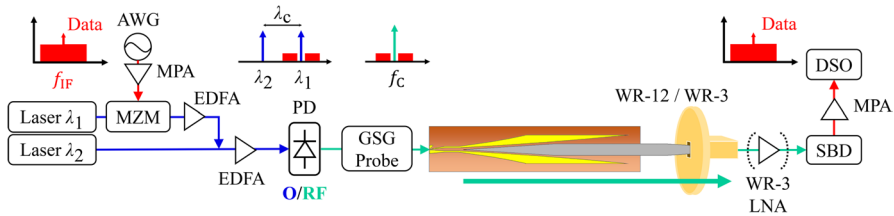
Fig. 9 Communication experiment at (**a**) 80 GHz and (**b**) 310 GHz using the transition. MPA, medium power amplifier; MZM, Mach-Zehnder modulator; EDFA, erbium-doped fiber amplifier; AWG, arbitrary waveform generator; UTC-PD, uni-traveling-carrier photodiode; GSG, ground-signal-ground; LNA, low noise amplifier; SBD, Schottky barrier diode; DSO, digital sampling oscilloscope. Optical, RF, and baseband/IF connections are shown in blue, green, and red, respectively. WR-3 LNA was used only in the experiment at the 300-GHz band

resulting signal is amplified by an EDFA and is combined with λ_2, functioning as a local optical oscillator, and is amplified to reach a power level of 12 dBm by a second EDFA. After passing through a polarization controller, it is fed into a PD to obtain the data signal at the carrier frequency $f_c = 80$ GHz. The output power from the PD module was approx. -15 dBm at minimum in the experiment. The GSG probe with an insertion loss of approx. 0.5 dB was attached to the PD, and the transition placed on the COC plate was fed with the GSG probe. The transition transferred the data signal into the DRW, with a linear taper inserted into the hollow waveguide. The hollow waveguide was connected to a Schottky barrier diode (SBD) detector (*VDI*, WR12ZBD-F), employing an envelope detection, and the signal was downconverted to IF. For demodulating the signal in the digital domain, after amplification at IF with MPA (*Miteq*, JS4-00102600), the waveform was digitized by a high-frequency digital sampling oscilloscope (DSO) (*Keysight*, DSA-Z 634A) and then analyzed using off-line DSP.

Figure 10 shows the measured bit error rates (BERs) as a function of modulation rates in (a) 4-QAM and (b) 16-QAM IF-OFDM transmissions. As can be seen in Fig. 10(a) and (b), BERs below 10^{-5} were achieved with 6-GHz and 3-GHz modulation bandwidths of 4-QAM and 16-QAM IF-OFDM signals, corresponding to transmission at 12 Gbps. Considering hard-decision and soft-decision forward error correction (HD-FEC, SD-FEC) thresholds of 3.8×10^{-3} and 2.0×10^{-2} [36], an error-free transmission was successfully demonstrated up to 15 and 16 Gbps with 4-QAM and up to 20 and 24 Gbps with 16-QAM modulations, respectively. The recovered constellations for the transmissions achieving BER below 10^{-5} are presented in Fig. 11(a) and (c). Figure 11(c) and (d) show the recovered constellations for the transmission achieving BERs below the SD-FEC limit with different modulation schemes.

The main factor limiting the achieved data rate was the total bandwidth in the THz interconnection, consisting of the PD, the GSG probe, the transition, the DRW, and the SBD detector, which was approximately 8 GHz from the carrier frequency of 80 to 88 GHz, closely reaching the cutoff frequency of WR-12 components at 90 GHz. Therefore, a fully integrated THz interconnect without
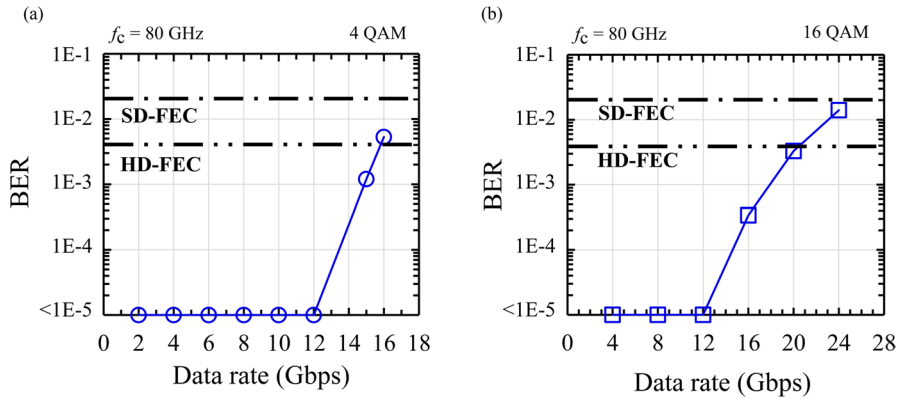
Fig. 10 (Bit error rates) BERs as a function of demonstrated data rate in (**a**) 4-QAM and (**b**) 16-QAM IF-OFDM transmissions 80-GHz band. Soft-decision and hard-decision forward error correction (SD-FEC, HD-FEC) thresholds are 2.0×10^{-2} and 3.8×10^{-3}, respectively
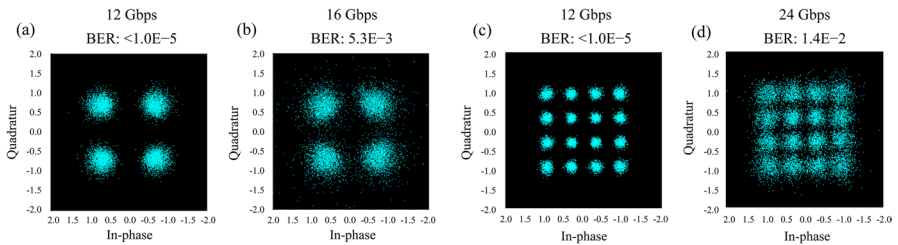

Fig. 11 Recovered constellation diagrams in 80-GHz band 4-QAM IF-OFDM signals at (**a**) 12 and (**b**) 16 Gbps and 16-QAM IF-OFDM signals at (**c**) 12 and (**d**) 24 Gbps. Data rates and BERs are shown on the top of each constellations

WR could offer a wider bandwidth, leading to a higher data rate in single-channel transmission or a higher data rate in multiple-channel transmissions.

5.2 DRW Interconnects at 300-GHz Band

As with the communication at 80 GHz, we also demonstrate the data interconnect at 310 GHz using the same IF-ODFM schemes. The block diagram of the experimental setup is illustrated in Fig. 9. To demonstrate the communication at the 300-GHz band, the J-band UTC-PD module and WR-3 GSG probe were used at the transmitter side. At the receiving side, we employed the WR-3 SBD detector and WR-3 LNA used in the transition characterization, as described in Section 4.2. The carrier frequency f_c and the IF frequency f_{IF} were set as 310 GHz and 6 GHz, respectively. The same conditions were implemented for the other setups in the communications at the 80-GHz band. Figure 12 shows the demonstrated BER as a function of the achieved data rate and the recovered constellation diagrams in 4-QAM IF-OFDM signal interconnection at the 300-GHz band.
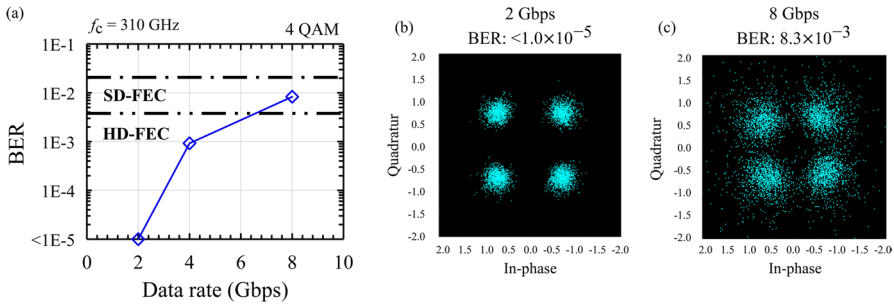
Fig. 12 BERs as a function of demonstrated data rate in (**a**) 4-QAM IF-OFDM transmissions at 300-GHz band. Soft-decision and hard-decision forward error correction (SD-FEC, HD-FEC) thresholds are 2.0×10^{-2} and 3.8×10^{-3}, respectively [36]. Recovered constellation diagrams in 4-QAM IF-OFDM signals at 300-GHz band at (**b**) 2 and (**c**) 8 Gbps

As can be seen in Fig. 12(a), we successfully demonstrated a 2-Gbps 4-QAM IF-OFDM signal transmission with BER below 10^{-5} and error-free transmission of up to 8 Gbps data rate with BER below the SD-FEC limit. The key results performed with the DRW interconnects at the 80-GHz and the 300-GHz band are summarized in Table 2. The maximum data rate was limited because of the low signal-to-noise ratio (SNR) in the 300-GHz band transmission system. It is essential to mention that the output power from the UTC-PD we used in the experiment was as low as -35 dBm at around 310 GHz. Therefore, without an additional amplifier having a 28-dB gain and 11-dB noise figure at the receiver side, the SBD detector could not detect the transferred signal through the GSG probe and the interconnect. Significant progress could be expected concerning a higher SNR when considering the monolithic integration of InP-based UTC-PD and the transition. A monolithically integrated transition with a high-output UTC-PD [15] could enable an UWB operation from WR-12, starting at 60 GHz, up to beyond the WR-3 frequency band for a higher-speed THz interconnection. Table 3 summarizes the state-of-the-art HR-Si waveguide interconnects for planar integration of active devices. Compared with the other notable work, the fabricated HR-Si DRW interconnect with InP-based transition presents quite wide relative bandwidth and a number of WR operational bands covering from WR-12 to WR-3 with a compatible insertion loss per transition. Furthermore, the fabricated interconnect demonstrated high-speed interconnections at multiple frequency bands toward multi-band communication applications.

Table 2 DRW interconnects results ([*] indicates below SD-FEC limit)

Data rate	f_c	Modulation	BER
24 Gbps	80 GHz	16 QAM	1.4E–02 [*]
16 Gbps	80 GHz	4 QAM	5.3E–03 [*]
12 Gbps	80 GHz	16 QAM	< 1.0E–05
12 Gbps	80 GHz	4 QAM	< 1.0E–05
8 Gbps	310 GHz	4 QAM	8.3E–03 [*]
2 Gbps	310 GHz	4 QAM	< 1.0E–05

Table 3 State-of-the-art HR-Si waveguide interconnects for planar integration

Ref	Transition technology	Covered WR	3-dB BW	Relative bandwidth	Center frequency	Min. IL per transition	Data rate @ f_c	BER
[37]	Vertical coupling between MSL on BCB and Si DRW	WR-5	20/55 GHz	11/31%	175 GHz	3.3/3.2 dB	10 Gbps	<1.0E−12
[27]	End-fire coupling between InP-RTD integrated with tapered-slot antenna and Si photonic crystal waveguide	WR-2.8	50 GHz	14%	340 GHz	0.45 dB	32 Gbps @350 GHz z	2.0E−12
							36 Gbps @350 GHz	<2.0E−3
[38]	Near-field coupling between Si DRW on HDPE and PCA integrated with tapered-slot antenna on HDPE	WR-1.9 WR-1.5 WR-1.0	440 GHz	57%	770 GHz	2 dB	-	-
[39]	Near-field coupling between MSL on Quartz and Si DRW	WR-6 WR-5	100 GHz	59%	170 GHz	1.75 dB	12 Gbps @140 GHz	<1.0E−12
							10 Gbps @180 GHz	<1.0E−12
This work	Near-field coupling between CPW on InP and Si DRW	WR-12 WR-10 WR-8 WR-6 WR-5	185 GHz	114%	157.5 GHz	2 dB	24 Gbps @80 GHz	1.4E−2
							8 Gbps @310 GHz	8.3E−3

6 Conclusion

We demonstrate an UWB multi-octave THz interconnect technology using planar InP-based transitions to couple THz signals from CPWs to low-loss Si DRWs. The fabricated interconnects support multi-octave operation from the millimeter wave frequency band (WR-12) to beyond the WR-3 THz frequency band. A maximum coupling efficiency of better than -2 dB is achieved from 80 to 170 GHz. The measured 3-dB and 6-dB operational bandwidths are 185 and 280 GHz, respectively. This corresponds to record bandwidths of 114% and 140%. The coupling efficiency is mainly limited due to the radiation loss of the transition, caused by the excitation of substrate modes in the 100-μm-thick InP substrate and high-order modes that interfere with the fundamental mode in the 500-μm-thick Si DRW. The coupling efficiency could be further improved by introducing a thinner InP substrate and a thinner Si DRW. Furthermore, as a proof of concept, we demonstrated multi-band IF-OFDM-based THz communications using the same fabricated THz interconnect for WR-12 and WR-3 bands. Error-free 16-QAM IF-OFDM 24 Gbps signal transmission at 80 GHz is achieved assuming soft-decision forward error correction (SD-FEC). At 310 GHz, despite the low output power available from the commercial PD, we achieved 4-QAM IF-OFDM 8 Gbps signal transmission for SD-FEC. Future monolithic integration of InP-based UTC-PDs with the proposed transition would eliminate the use of WR transitions which are currently limiting the operational RF bandwidth, and pave the way toward multi-band and UWB THz communications.

Author Contribution S. Iwamatsu wrote the main manuscript text and prepared all figures. All authors reviewed the manuscript.

Data Availability Data underlying the results presented in this paper are not publicly available at this time but may be obtained from the authors upon reasonable request.

Declarations

Ethical Approval Not applicable

Competing Interests The authors declare no competing interests.

References

1. Cisco, U. "Cisco annual internet report (2018–2023) white paper," Cisco: San Jose, CA, USA, (2020). [Online] Available: https://www.cisco.com/c/en/us/solutions/collateral/executive-perspectives/annualinternet-report/white-paper-c11-741490.pdf

2. T. Nagatsuma, G. Ducournau, and C. C. Renaud, "Advances in terahertz communications accelerated by photonics," Nature Photon., 10, 371–379 (2016).

3. S. S. Dhillon, M. Vitiello, and E. Linfield, et al., "The 2017 terahertz science and technology roadmap," J. Phys. D: Appl. Phys., 50, 043001 (2017).

4. T. Kürner, D. M. Mittleman, and T. Nagatsuma, "Introduction to THz Communications," Springer Ser. Opt. Sci. 234, 1–12 (2022).

5. H. Matsumoto, I. Watanabe, A. Kasamatsu, and Y. Monnai, "Integrated terahertz radar based on leaky-wave coherence tomography," Nat. Electron., 3, 122–129 (2020).

6. F. Zhang, Q. Guo, and S. Pan, "Photonics-based real-time ultra-high-range-resolution radar with broadband signal generation and processing," Sci. Rep, 7, 13848 (2017).

7. L. Yi, R. Kaname, R. Mizuno, Y. Li, M. Fujita, H. Ito, and T. Nagatsuma, "Ultra-Wideband Frequency Modulated Continuous Wave Photonic Radar System for Three-Dimensional Terahertz Synthetic Aperture Radar Imaging," J. Lightw. Technol., 40, 6719–6728 (2022).

8. L. Liebermeister, S. Nellen, R. B. Kohlhaas, S. Lauck, M. Deumer, S. Breuer, M. Schell, and B. Globisch, "Optoelectronic frequency-modulated continuous-wave terahertz spectroscopy with 4 THz bandwidth," Nat. Commun., 12, 1–10 (2021).

9. J. Seddon, C. Graham, M. Georgiades, C. Renaud, and A. Seeds, "An On-Chip Continuous Wave Terahertz Spectrometer," arXiev preprint arXiv: 2212.02215 (2022).

10. S. Dülme, N. Schrinski, B. Khani, P. Lu, V. Rymanov, A. Stöhr, C. Brenner, and M. R. Hofmann, "Compact optoelectronic THz frequency domain spectroscopy system for refractive index determination based on Fabry-Perot effect," in 2018 First International Workshop on Mobile Terahertz Systems (IWMTS), 1–5 (2018).

11. T. Ishibashi, N. Shimizu, S. Kodama, H. Ito, T. Nagatsuma and T. Furuta, "Uni-traveling-carrier photodiodes," Tech. Dig. Ultrafast Electronics Optoelectronics OSA Spring Topical Meeting, 166–168 (1997).

12. J. P. Seddon, M. Natrella, X. Lin, C. Graham, C. C. Renaud, and A. J. Seeds, "Photodiodes for Terahertz Applications," IEEE J. Sel. Top. Quantum Electron., 28, 1–12 (2022).

13. D. Fukuoka, K. Muro, and K. Noda, "Coherent THz light source based on photo-mixing with a UTC-PD and ASE-free tunable diode laser," Proc. SPIE 9747, Terahertz, RF, Millimeter, and Submillimeterc Wave Technology and Applications IX, 974717 (2016).

14. B. Khani, S. Makhlouf, A. G. Steffan, J. Honecker, and A. Stöhr, "Planar 0.05–1.1 THz Laminate-Based Transition Designs for Integrating High-Frequency Photodiodes With Rectangular Waveguides," J. Lightw. Technol., 37, 1037–1044 (2019).

15. S. Makhlouf, J. Martinez-Gil, M. Grzeslo, D. Moro-Melgar, O. Cojocari, and A. Stöhr, "High-power UTC-photodiodes for an optically pumped subharmonic terahertz receiver," Opt. Express, 30, 43798–43814 (2022).

16. M. Grzeslo, S. Dülme, S. Clochiatti, T. Neerfeld, T. Haddad, P. Lu, J. Tebart, S. Makhlouf, C. Biurrun-Quel, J. L. Fernández Estévez, J. Lackmann, N. Weimann, and A. Stöhr, "High saturation photocurrent THz waveguide-type MUTC-photodiodes reaching mW output power within the WR3.4 band," Opt. Express, 31, 6484–6498 (2023).

17. K. Sengupta, T. Nagatsuma, and D. M. Mittleman, "Terahertz integrated electronic and hybrid electronic–photonic systems," Nat. Electron., 1, 622–635 (2018).

18. R. Han, Z. Hu, C. Wang, J. Holloway, X. Yi, M. Kim, and J. Mawdsley, "Filling the Gap: Silicon Terahertz Integrated Circuits Offer Our Best Bet," IEEE Microw. Mag., 20, 80–93 (2019).

19. A. Kumar, M. Gupta, P. Pitchappa, N. Wang, M. Fujita, and R. Singh, "Terahertz topological photonic integrated circuits for 6G and beyond: A Perspective," J. Appl. Phys., 132, 140901 (2022).

20. A. Rivera-Lavado, S. Preu, L. E. Garcia-Munoz, A. Generalov, J. Montero-De-Paz, G. Dohler, D. Lioubtchenko, M. Mendez-Aller, F. Sedlmeir, M. Schneidereit, H. G. L. Schwefel, S. Malzer, D. Segovia-Vargas, and A. V. Raisanen, "Dielectric Rod Waveguide Antenna as THz Emitter for Photomixing Devices," IEEE Trans. Antennas Propag., 63, 882–890 (2015).

21. A. Malekabadi, S. A. Charlebois, D. Deslandes, and F. Boone, "High-Resistivity Silicon Dielectric Ribbon Waveguide for Single-Mode Low-Loss Propagation at F/G-Bands," IEEE Trans. Terahertz Sci. Technol., 4, 447–453 (2014).

22. D. Headland, W. Withayachumnankul, X. Yu, M. Fujita, and T. Nagatsuma, "Unclad Microphotonics for Terahertz Waveguides and Systems," J. Lightwave Technol., 38, 6853–6862 (2020).

23. M. Ali, J. Tebart, A. Rivera-Lavado, D. Lioubtchenko, L. E. Garcia-Muñoz, A. Stöhr, and G. Carpintero, "Terahertz Band Data Communications using Dielectric Rod Waveguide," Optical Fiber Communication Conference (OFC), W1H-5, (2022).

24. D. Headland, W. Withayachumnankul, M. Fujita, and T. Nagatsuma, "Gratingless integrated tunneling multiplexer for terahertz waves," Optica, 8, 621 (2021).

25. S.A. Hosseini Farahabadi, M. Entezami, H. Abouali, H. Amarloo, M. Poudineh, and S. Safavi-Naeini, "Sub-terahertz silicon-based on-chip absorption spectroscopy using thin-film model for biological applications," Sci. Rep., 12, 1–9 (2022).

26. D. Headland, M. Ali, D. C. Gallego, and G. Carpintero, "Broadband liquid sensing of sealed microfluidic channel using mm-wave dielectric rod waveguide," in 2022 47th International Conference on Infrared, Millimeter, and Terahertz waves (IRMMW-THz), 1–2 (2022).

27. X. Yu, J.-Y. Kim, M. Fujita, and T. Nagatsuma, "Efficient mode converter to deep-subwavelength region with photonic-crystal waveguide platform for terahertz applications," Opt. Express, 27, 28707-28721 (2019).

28. S. Iwamatsu, M. Ali, J. L. Fernandez-Estevez, S. Makhlouf, G. Carpintero, and A. Stöhr, "Broadband THz Interconnect for Hybrid Integration of InP and Si Platforms," in 2022 47th International Conference on Infrared, Millimeter, and Terahertz waves (IRMMW-THz), 1–2 (2022).

29. I. Mohammad, "Photonic Non-Invasive mmW and THz Imaging for Non-Melanoma Skin Cancer Detection," in 2022 5th International Workshop on Mobile Terahertz Systems (IWMTS), 1–5 (2022).

30. H. Hamada, T. Kosugi, H.-J. Song, M. Yaita, A. E. Aoutaouakil, H. Matsuzaki, and A. Hirata, "300-GHz Band 20-Gbps ASK Transmitter Module Based on InP-HEMT MMICs", 2015 IEEE Compound Semiconductor Integrated Circuit Symposium (CSICS), 1–2 (2015).

31. P. Lu, T. Haddad, B. Sievert, B. Khani, S. Makhlouf, S. Dulme, J. F. Estevez, A. Rennings, D. Erni, U. Pfeiffer, and A. Stöhr, "InP-Based THz Beam Steering Leaky-Wave Antenna," IEEE Trans. Terahertz Sci. Technol., 11, 218–230 (2021).

32. Evonik Operations GmbH, "ROHACELL® HF Product Information," Evonik Operations GmbH: Darmstadt, Germany, Apr. (2022). [Online] Available: https://products.evonik.com/assets/52/54/Asset_1255254.pdf (accessed on 27 June 2023)

33. TOPAS Advanced Polymers GmbH, "TECHNICAL DATA SHEET – TOPAS 5013L-10," Cisco: Raunheim, Germany, Jul. (2019). [Online] Available: https://topas.com/sites/default/files/TDS_5013L-10_e.pdf (accessed on 27 June 2023)

34. A. Rivera-Lavado, M. Ali, D. Gallego-Cabo, L. -E. García-Muñoz, D. Lioubtchenko and G. Carpintero, "Contactless RF Probe Interconnect Technology Enabling Broadband Testing to the Terahertz Range," IEEE Trans. Terahertz Sci. Technol., 14, 1–10 (2022).

35. M. Hermelo, P. Shih, M. Steeg, A. Ng'oma, and A. Stöhr, "Spectral efficient 64-QAM-OFDM terahertz communication link," Opt. Express, 25, 19360–19370 (2017).

36. S.-R. Moon, M. Sung, J. K. Lee, and S.-H. Cho, "Cost-Effective Photonics-Based THz Wireless Transmission Using PAM-N Signals in the 0.3 THz Band", J. Lightw. Technol., 39, 357–362 (2021).

37. . Yu, Y. Ye, X. Ding, Y. Liu, Z. Xu, X. Liu, and Q. J. Gu, "Ortho-Mode Sub-THz Interconnect Channel for Planar Chip-to-Chip Communications", IEEE Trans. Microw. Theory Tech., 66, 1864–1873 (2018).

38. A. K. Mukherjee, M. Xiang, and S. Preu, "Broadband Terahertz Photonic Integrated Circuit with Integrated Active Photonic Devices," Photonics, 8, 492 (2021).
39. X. Ding, B. Yu, Y. Ye, H. Yu, Z. Xuand Q. Jane Gu, "An FDD-based Full-Duplex Sub-THz Interconnect with Data-rate of 22.6 Gb/s and Energy-Efficiency of 1.58pJ/bit," in 2021 46th International Conference on Infrared, Millimeter and Terahertz Waves (IRMMW-THz), 1–2 (2021).

Publisher's Note Springer Nature remains neutral with regard to jurisdictional claims in published maps and institutional affiliations.